Multiphysics Model of Metal Solidification on the Continuum Level

Seid Koric[a], Lance C. Hibbeler[b], Rui Liu[b], Brian G. Thomas[b]

[a] *National Center for Supercomputing Applications, University of Illinois, Urbana, IL, 61801*

[b] *Department of Mechanical Science and Engineering, University of Illinois, Urbana, IL, 61801*

Abstract

Separate three-dimensional (3-D) models of thermo-mechanical behavior of the solidifying shell, turbulent fluid flow in the liquid pool, and thermal distortion of the mold are combined to create an accurate multiphysics model of metal solidification at the continuum level. The new system is applied to simulate continuous casting of steel in a commercial beam-blank caster with complex geometry. A transient coupled elastic-viscoplastic model (Koric and Thomas, 2006) computes temperature and stress in a transverse slice through the mushy and solid regions of the solidifying metal. This Lagrangian model features an efficient numerical procedure to integrate the constitutive equations of the delta-ferrite and austenite phases of solidifying steel shell using a fixed-grid finite-element approach. The Navier-Stokes equations are solved in the liquid pool using the standard K-ε turbulent flow model with standard wall laws at the mushy zone edges that define the domain boundaries. The superheat delivered to the shell is incorporated into the thermal-mechanical model of the shell using the enhanced latent heat method (Koric et al., 2010). Temperature and thermal distortion modeling of the complete complex-shaped mold includes the tapered copper plates, water cooling slots, backing plates, and nonlinear contact between the different components. Heat transfer across the interfacial gaps between the shell and the mold is fully coupled with the stress model to include the effect of shell shrinkage and gap formation on lowering the heat flux. The model is validated by comparison with analytical solutions of benchmark problems of conduction with phase change (Dantzig and Tucker, 2001), and thermal stress in an unconstrained solidifying plate (Weiner and Boley, 1963). Finally, results from the complete system compare favorably with plant measurements of shell thickness.

Keywords: Solidification, Mutiphysics, Thermal-Stress, Fluid Flow, Superheat, Viscoplastic, Turbulence, Continuous Casting

1. Introduction and Previous Work

Many manufacturing processes, such as foundry casting, continuous casting, and welding, are governed by multiple coupled phenomena which include turbulent fluid flow, heat transfer, solidification, distortion, and stress generation. The difficulty of plant experiments under harsh operating conditions makes computational modeling an important tool in the design and optimization of these processes. Increased computing power and better numerical methods have enabled researchers to develop better models of many different aspects of these processes. Coupling together the different models of the different phenomena to make accurate predictions of the entire real processes remains a challenge.

In early work (Weiner and Boley, 1963) a semi-analytical solution was derived for the thermal stresses arising during the solidification of a semi-infinite plate. Although that work oversimplifies the complex physical phenomena of solidification, it has become a useful benchmark problem for the verification of numerical models. The constitutive models used in previous models of thermal stresses during continuous casting first adopted simple elastic-plastic laws (Weiner and Boley 1963, Grill *et al*., 1976) and simple creep laws (Rammerstrofer *et al*., 1979, Kristiansson, 1984). With improving computer hardware, more computationally challenging elastic-viscoplastic models have been used (Zhu 1993, Boehmer *et al*., 1998, Li and Thomas, 2004, Risso *et al*., 2006, Koric and Thomas, 2006). While the Lagrangian description of this process with a fixed mesh is widely adopted due to its easy implementation, an alternative mechanical model based on an arbitrary Eulerian-Lagrangian description has been implemented as well (Risso *et al*., 2006). To enable fast convergence of the highly-nonlinear constitutive equations that accompany solidification and high-temperature deformation, a robust local viscoplastic integration scheme (Zhu, 1993, Li and Thomas 2004) has been implemented (Koric and Thomas, 2006) into the commercial finite element package ABAQUS (Dassault Corp., 2009) via its user defined material subroutine UMAT, including special treatment of liquid/mushy zone. This enables realistic computational modeling of complex solidification processes with ABAQUS (Koric *et al*., 2009, Hibbeler *et al*., 2009).

As the demand for better computer simulations of solidification processes increases, there is a growing need to include the effects of fluid flow into thermo-mechanical analyses. The multiphysics approach of simulating all three macroscale phenomena (i.e. fluid flow, solidification heat transfer, and mechanical distortion) simultaneously has been demonstrated in several previous works,(ref cross, others??) but is very computationally demanding for realistic problems. Major difficulties stem from the inherently different coordinate descriptions and numerical techniques used in the separate models for these three fields. Fluid flow typically is performed on structured Eulerian domains using steady-state control-volume methods with iterative solution algorithms. Stress analysis typically is performed on unstructured

Lagrangian domains using transient finite-element methods with direct solvers. Many different methods are used to treat heat transfer with moving solidification front(s).(Voller review??) Further difficulties arise from the complex geometries, which require large computational meshes.

Lee and coworkers (Lee *et al*., 2000) showcased multiphysics modeling by coupling a 3-D finite-difference model of fluid flow with a 2-D transient thermal-stress model to predict solidification, gap formation, stress, and crack formation in a beam-blank caster. Teskeredzic *et al*. (Teskeredzic *et al*., 2002) used a 2D multiphysics finite-volume method for simultaneous prediction of physical phenomena during a solid/liquid phase change. Neither prediction was validated with plant measurements. Some researchers attempted to decouple the thermal-fluid simulation from the stress analysis (Shamsi *et al*., 2008, Pokorny *et al*., 2008) but this neglects the important effects of shrinkage and deformation on heat transfer, such as that caused by increased pressure or gap formation between the casting and the mold (Ho and Pehlke, 1985).

Alternatively, the fluid flow simulation can be reasonably decoupled from the thermal-stress analysis if the liquid pool shape can be estimated a-priori and the mechanical influence of fluid on the solid shell is modeled with hydrostatic pressure boundary conditions. Doing so is relatively easy for many processes involving a stable interface shape, such as ledge formation in cryolite electrolysis or the continuous casting of steel. Such simulations can readily output the "superheat flux" that delivers heat to the solidification front, such as characterized by the liquidus temperature. Recently Koric *et al*. (Koric *et al*., 2010) has demonstrated that "superheat flux" can be incorporated into a transient simulation of heat transfer phenomena in the mushy and solid regions by enhancing the latent heat in the mushy zone without an explicit need to track the solidification front. The procedure has been added into the commercial package ABAQUS (Dassault Corp., 2009) with a user-defined subroutine UMATHT. In the present work, this approach is applied to perform a realistic simulation of turbulent fluid flow, heat transfer, solidification, stress, and mold distortion of a commercial beam-blank caster.

The continuous casting process used here to exemplify multiphysics modeling is used to produce nearly all of the steel in the world. The process empties ladles of molten steel through a vessel called a tundish, which stores steel between changes and also helps to clean the metal. The tundish drains into a bottomless, water-cooled copper mold, which extracts heat from the molten steel and solidifies a shell. The shell is withdrawn at a rate called the casting speed into a region of water sprays, which complete the solidification. Slabs are then cut to the desired length and sent for downstream processing, such as rolling. The molds produce thick or thin slabs, square billets, blooms, rounds, and also near-net-shape

"beam blank" or "dogbone" cross-sections. Fig. 5 shows a cross section of a typical beam blank caster. The computational models developed in this paper exploit the two-fold symmetry of the mold.

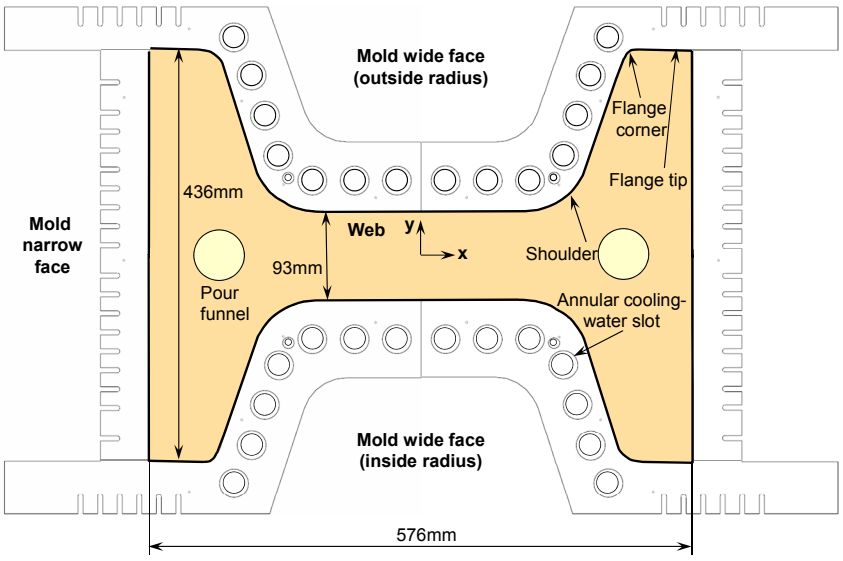

Figure 5: Schematic of beam blank caster (top view)

2. Governing Equations

The conservation of mass, momentum, and energy (Dantzig and Tucker, 2001) are satisfied in the molten metal, solidifying shell, and solid mold using three different models and three different computational domains. Mass conservation for a material with constant density can be expressed mathematically as:

$$\rho\left(\nabla\cdot\boldsymbol{v}\right)=0 \tag{1}$$

where ρ is the mass density and $\boldsymbol{v}$ is velocity. Momentum conservation is satisfied by solving a version of the following static mechanical equilibrium equation without body forces in each model:

$$\rho\left[\frac{\partial\boldsymbol{v}}{\partial t}+\boldsymbol{v}\cdot\left(\nabla\boldsymbol{v}\right)\right]=\nabla\cdot\boldsymbol{\sigma} \tag{2}$$

where $\boldsymbol{\sigma}$ is the Cauchy stress tensor. Boundary conditions are either fixed displacement/velocity, or surface tractions applied in the form of normal pressure and tangential shear stresses. Each model also solves the following energy conservation equation, for a system without viscous dissipation and internal heat sources:

$$\rho\left[\frac{\partial H}{\partial t}+\boldsymbol{v}\cdot\nabla H\right]=\nabla\cdot\left(\boldsymbol{k}\cdot\nabla T\right) \tag{3}$$

where H is temperature-dependent specific enthalpy that includes the latent heat of solidification, T is temperature, $\boldsymbol{k}$ is the temperature-dependent thermal conductivity tensor, simplified in all domains to $k\boldsymbol{I}$ by assuming isotropy. Boundary conditions are either prescribed temperatures or heat flux, the latter often in the form of a convection condition.

3. Solidifying Shell Model

The solidifying steel shell is modeled as a transverse Lagrangian slice that moves down through the mold at the casting speed. Because the domain and material velocities are identical, the Lagrangian formulation removes the advection terms from the governing equations. This is a slight oversimplification because the mushy zone does not move at exactly the casting speed. Eq. 1 is satisfied by use of the Lagrangian formulation, and the effect of the temperature-dependence of the mass density is manifested as thermal strain. Gravity is negligible relative to the thermal loading, so there is no body force term in Eq. 2. The deformation rates in the solid shell are small, so the inertia terms may be safely neglected. Eq. 2 then simply demands that the stress tensor be divergence-free. The constitutive relationship for solid metals is expressed by the rate form of Hooke's law:

$$\dot{\boldsymbol{\sigma}}=\mathbb{C}:\left(\dot{\boldsymbol{\varepsilon}}-\dot{\boldsymbol{\varepsilon}}^{th}-\dot{\boldsymbol{\varepsilon}}^{ie}\right) \tag{4}$$

where $\mathbb{C}$ is the fourth-order tensor of elastic constants assumed here to be isotropic, $\dot{\boldsymbol{\varepsilon}}^{th}$ is the thermal strain rate tensor calculated from temperatures resulting from the solution of Eq. 3, $\dot{\boldsymbol{\varepsilon}}^{ie}$ is the inelastic strain rate tensor, and $\dot{\boldsymbol{\varepsilon}}$ is the total linearized strain rate tensor, calculated from:

$$\dot{\boldsymbol{\varepsilon}}=\frac{d}{dt}\left[\frac{1}{2}\left(\nabla\boldsymbol{u}+\left(\nabla\boldsymbol{u}\right)^{T}\right)\right] \tag{5}$$

where $\boldsymbol{u}$ is the displacement vector. Note that this formulation does not include the effect of the temperature dependence of the elastic constants on the stress rate. This small-strain mechanical model is reasonable for casting processes.

The governing equations are incrementally solved using the finite-element method in ABAQUS using a fully implicit stepwise-coupled algorithm for the time integration of the governing equations (Dassault Corp., 2009). The highly-nonlinear constitutive laws are integrated by solving a system of ordinary

differential equations defined at each material point using the backward-Euler method with a bounded Newton-Raphson method (Koric and Thomas, 2006) in the user subroutine UMAT. In each time step the thermal problem is first solved, and then the resulting thermal strains are used to drive the mechanical problem. Global Newton-Raphson iterations continue until tolerances for both equation systems are satisfied before proceeding to the next time step.

Temperature- and phase-dependent enthalpy, thermal conductivity, thermal expansion, and elastic modulus (Hibbeler et al., 2009) were calculated for 0.071 % wt. C plain carbon steel with T_{sol} = 1471.9 ºC and T_{liq} = 1518.7 ºC. The volume fractions of the liquid, delta, and austenite phases are calculated according to a linearized phase diagram [ref Won??]. Other simulation conditions are listed in Table II.

The inelastic strain includes both strain-rate independent plasticity and time-dependent creep. Creep is significant at the high temperatures of the solidification processes and is indistinguishable from plastic strain. The following unified constitutive equation (Kozlowski *et al*., 1992) defines inelastic strain in the solid austenite phase:

$$\dot{\bar{\varepsilon}}_{ie}[\mathrm{sec}^{-1}] = f_C\left(\bar{\sigma}[\mathrm{MPa}] - f_1\,\bar{\varepsilon}_{ie}\,|\,\bar{\varepsilon}_{ie}\,|^{f_2-1}\right)^{f_3}\exp\left(-\frac{Q}{T[K]}\right)$$

$$\begin{aligned}&\text{where:}\\ &Q = 44,465\\ &f_1 = 130.5 - 5.128\times10^{-3}\,T\,[\mathrm{K}]\\ &f_2 = -0.6289 + 1.114\times10^{-3}\,T\,[\mathrm{K}]\\ &f_3 = 8.132 - 1.54\times10^{-3}\,T\,[\mathrm{K}]\\ &f_C = 46,550 + 71,400\,(\%C) + 12,000\,(\%C)^2\end{aligned} \qquad (6)$$

where Q is an activation energy, and f_1, f_2, f_3, f_C are empirical temperature- and composition-dependant constants. The modified power-law model developed by Zhu (Zhu, 1993) is used to simulate the delta-ferrite phase, which exhibits significantly higher creep rates and lower strength than the austenite phase. The delta-ferrite constitutive model is used whenever the volume fraction of ferrite is greater than 10%. To enforce negligible liquid strength in mushy and liquid zones before solidification takes place, an isotropic elastic-perfectly-plastic rate-independent constitutive model is used when the temperature is above the solidus temperature. The yield stress $\sigma_Y = 0.01\mathrm{MPa}$ is chosen small enough to effectively eliminate stresses in the liquid-mushy zones, but also large enough to avoid computational difficulties.

The Lagrangian shell-model domain given in Fig. 6, was discretized with 32874 nodes and 63,466 degrees of freedom, and required 12409 time steps for the complete 45-s simulation down the mold length. It encompasses corresponding thin "stripe" of the strand section adjacent to the mold wall, which is wide enough to allow solidification of the expected shell everywhere. This avoids expensive computation in the larger liquid domain with the thermo-mechanical model. More importantly, the enclosed space which represents the internal liquid cavity is able to shrink to properly model liquid feeding of the real continuous casting process.

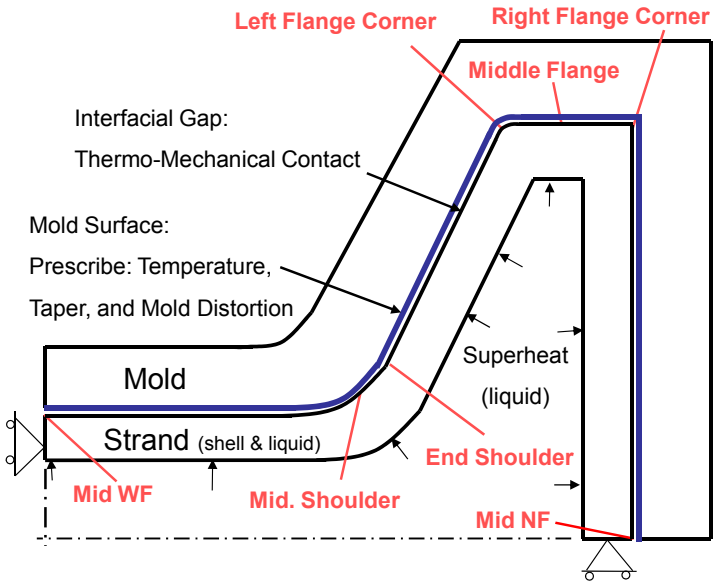

Figure 6.5: Shell model domain with thermo-mechanical boundary conditions

This 2-D transient model also comprises a 3-D solution at steady state. The slice begins at the top of the liquid steel pool, where the uniform initial conditions are the pouring temperature, T_0, zero displacement, zero strain, and zero stress. The 2-D assumption is valid for the thermal analysis, owing to negligible axial conduction, as shown with the large Peclet number $\mathrm{Pe} = V_c L/\alpha \approx 10^5$, where V_c is the casting speed, L is mold length, and α is thermal diffusivity (Dantzig and Tucker, 2001). The appropriate two-dimensional mechanical state is that of generalized plane strain with negligible out-of-plane bending, which has been shown capable of reproducing the complete 3-D stress state (Explicit paper??).

4. Fluid Flow Model

A 3-D fluid flow model of the liquid pool of molten steel solves for the time-averaged velocity and pressure distributions in an Eulerian domain. The fluid flow model is constructed for an incompressible Newtonian fluid, so Eq. 1 simplifies to a divergence-free velocity field, and the constitutive relationship for the Cauchy stress tensor in Eq. 2 is:

$$\boldsymbol{\sigma} = C_{\mu}\frac{K^2}{\in}\left(\nabla \boldsymbol{v} + (\nabla \boldsymbol{v})^T\right) - p\boldsymbol{I} \tag{7}$$

where p is pressure, constant C_{μ} is 0.09, and the turbulent kinetic energy K, and its dissipation $\in$, are found by solving two additional transport equations using the standard K-$\in$ model (Launder and Spalding, 1974) for turbulence. Buoyancy forces are negligible relative to the flow inertia, as indicated by $Gr/Re^2 \sim 10^{-2}$-10^{-4}, where Gr is the Grashoff number and Re is the Reynolds number. The velocity and temperature fields are thus decoupled, as the flow affects the temperature but the temperature does not affect the flow. The governing equations are solved using the finite-volume method with the SIMPLE method and first-order upwinding in FLUENT (Ansys Inc., 2008), as explained elsewhere (Versteeg and Malalasekera, 2008) to give the pressure, velocity, and temperature fields at each cell in the computational domain, and the heat flux at the domain boundary surfaces.

The shape of the domain is specified by extracting the position of the solidification front (liquidus temperature) from the solidifying shell model, and the symmetry planes of the mold. Fluid enters the liquid pool through a funnel that catches the gravity-driven stream from the tundish bottom. This is modeled with fixed $\boldsymbol{v}$, K, and $\in$ on an appropriate circular inlet boundary plane on the top surface. Standard wall functions are used to model the steep velocity gradients near the shell-interface domain boundaries of this problem involving high Reynolds number (54,000 at nozzle). Symmetry planes are treated with the appropriate symmetry boundary conditions. Boundaries at the shell-liquid interface are given a vertical downward velocity fixed at the casting speed. The effect of shell growth is incorporated as mass and momentum sinks (Rietow, 2007) in a user-defined function (UDF) (Ansys Inc., 2008).

Fig. 7 shows the velocity and temperature distributions on the center planes and top plane (10-mm below the liquid surface) calculated with the 3D thermo-fluid flow simulation of 606,720 hexahedral cells. Table III has the input data used in this CFD analysis.

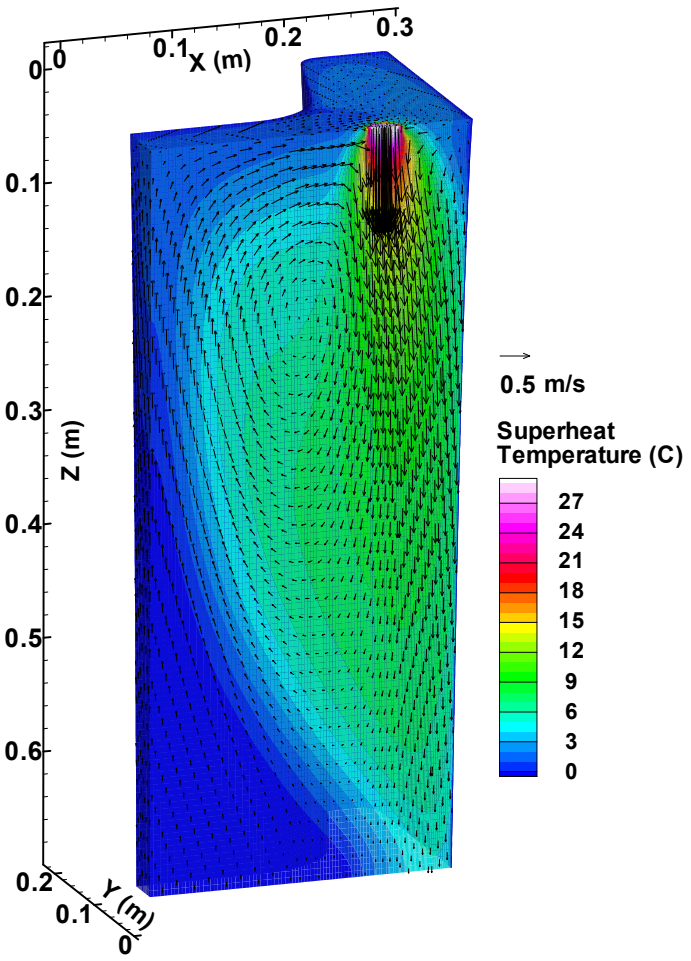

Figure 7: Velocity and Temperature Distributions in the Liquid Pool

5. Mold Model

In addition to supporting the shell to determine its shape, the copper mold in the continuous casting process extracts heat from the molten steel by means of cooling water flowing through circular channels and rectangular slots. The mold assembly consists of two wide faces, two narrow faces, and their respective water boxes. The steel water boxes serve to circulate the water in the mold and also increase the rigidity of the assembly to reduce the effect of the thermal distortion of the mold when it heats up to operating temperatures. In this work, a three-dimensional finite-element model of one symmetric fourth of the mold assembly was constructed to capture the effects of mold distortion and variable mold surface temperature on the solidifying steel shell. The model mold and water box geometries include the curvature and applied taper of the hot faces, water channels, and bolt holes. The taper is applied to the mold pieces to accommodate the solidification shrinkage of the solid steel.

The mesh consisted of 263,879 nodes and 1,077,166 tetrahedron, wedge, and hexahedron elements. The steady-state conservations of energy and momentum in Eqs. 2 and 3 were solved in this model using ABAQUS (Dassault Corp., 2009). The same constitutive relationship as the shell model was used for the mold, but the inelastic strain is neglected, owing to the minor role of creep in the copper towards mold distortion [ref.? G. Li copper paper Met Trans A 2001?]. Contact between the two mold pieces and two backing plates was enforced manually by iteratively applying constraint equations on contacting nodes. The mold bolts and tie rods were simulated using linear truss elements and were appropriately pre-stressed. The heat flux applied to the hot faces of the mold was extracted from the shell-mold surface in the shell model.

The calculated temperature and distortion results are presented in Figure 6. In addition to providing insight into thermo-mechanical behavior of the mold, this model provides temperature and displacement boundary conditions to the shell model. More detail of this model can be found elsewhere (Hibbeler *et al.*, 2009).

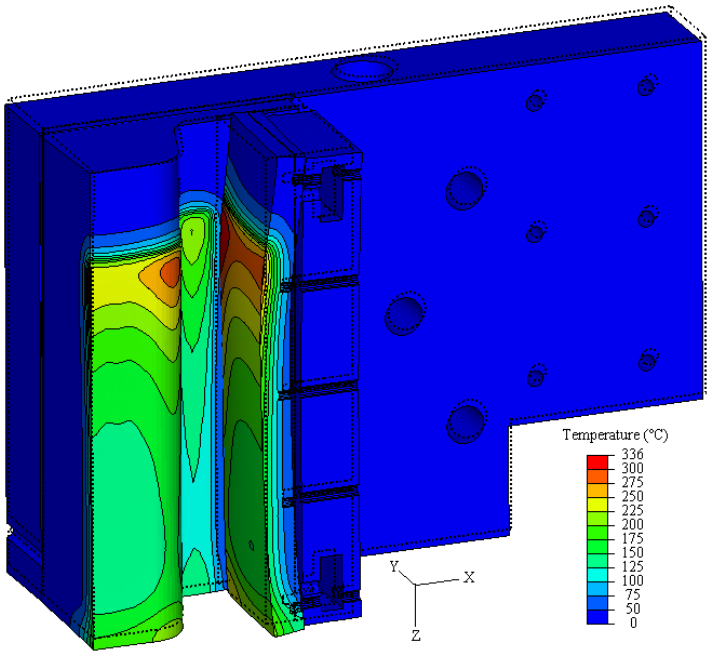

Figure 6. Temperature and distorted shape of mold (20x magnified distortion)

6. Fluid / Shell Interface Treatment

Results from the fluid flow model of the liquid domain affect the solidifying shell model by the heat flux crossing the boundary, which represents the solidification front, or liquidus temperature. This "superheat flux" q_{super} can be incorporated into a fixed-grid simulation of heat transfer phenomena in the mushy and solid regions by enhancing the latent heat (Koric *et al.*, 2010) in Eq. 1. This enables accurate uncoupling of complex heat-transfer phenomena into separate simulations of the fluid flow region and the mushy-solid region. Starting with the Stefan interface condition (Dantzig and Tucker, 2001), the additional latent heat ΔH_f to account for superheat flux delivered from the liquid pool can be calculated from:

$$\Delta H_f = \frac{q_{super}}{\rho_{solid} \left| v_{interface} \right|} \tag{8}$$

The latent heat enhancement is added to the original latent heat and enthalpy in Eq. 3 via a UMATHT user subroutine in ABAQUS (Dassault Corp., 2009). In the transient shell model, the interface speed $v_{interface}$ can be estimated from the local cooling rate and temperature gradient at every time and material point near the solidification front.

$$v_{interface} = \frac{\dot{T}}{\left\| \nabla T \right\|} = \frac{\Delta T}{\Delta t} \frac{1}{\left\| \nabla T \right\|} \tag{9}$$

This method sometimes produces excessive and fluctuating latent heat values when temperature increments ΔT are driven to be very small by the global NR iterative solution procedures, particularly at early simulation times and when superheat flux is high. When the maximum latent heat enhancement reaches 30 to 40 times the initial value of the latent heat, the $v_{interface}$ estimate switches to an analytical solution (Koric *et al.*, 2010) based on the classical 1-D solid-control solidification solution (Dantzig and Tucker, 2001) with the addition of superheat:

$$c_{ps} \left(T_{liq} - T_{surf} \right) = \phi \exp\left(\phi^2 \right) \operatorname{erf}(\phi) \sqrt{\pi} \left(H_f + \frac{q_{super}}{\rho \sqrt{\alpha_s} \phi} \frac{1}{\sqrt{t}} \right) \tag{11}$$

The above equation is solved for ϕ for every time increment and velocity is calculated as:

$$v_{interface}(t) = \phi \sqrt{\alpha_s / t} \tag{12}$$

This method gives an accurate and smooth estimate of the interface velocity, and was shown to perform well in both one- and two-dimensional solidification problems (Koric *et al.*, 2010).

Fig. 9 shows a 3-D view of the superheat flux distribution on the shell interface calculated from the CFD turbulent flow model. The fluid flow causes uneven distribution of superheat fluxes that are greatest midway down the inner shoulder, and least in the flange and center of the wide face. These variations in turn cause local shell thinning and temperature changes, which affect the thermal stress behavior.

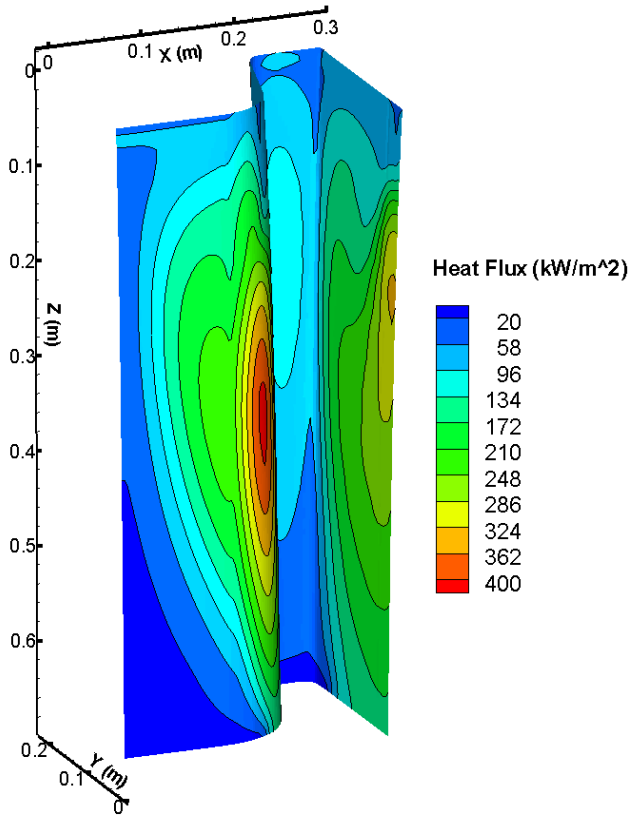

Figure 9: 3D view of the superheat flux distribution on the shell interface

The effect of the ferrostatic pressure in the liquid pool is treated in the shell model as a linearly-increasing distributed load that pushes the solidifying steel shell towards the mold. This boundary condition was treated using the ABAQUS user subroutine DLOAD.

7. Shell / Mold Interface Treatment

Two-way thermo-mechanical coupling between the shell and mold is needed because the stress analysis depends on temperature via thermal strains and material properties, and the heat conducted between the mold and steel strand depends strongly on distance between the separated surfaces calculated from the mechanical solution. Heat transfer across the interfacial gap between the shell and the mold wall surfaces is defined with a resistor model that depends on the thickness of gap calculated by the stress model. The total heat transfer q_{gap} occurs along two parallel paths, due to radiation, h_{rad}, and conduction, h_{cond}, as follows:

$$q_{gap} = -k\partial T / \partial n = -\left(h_{rad} + h_{cond}\right)\left(T_{shell} - T_{mold}\right) \tag{13}$$

where n is in the direction normal to the surface. The radiation heat transfer coefficient is calculated across the transparent liquid portion of the mold slag layer:

$$h_{rad} = \frac{\sigma_{SB}}{\dfrac{1}{\varepsilon_{shell}} + \dfrac{1}{\varepsilon_{mold}} - 1}\left(T_{shell} + T_{mold}\right)\left(T_{shell}^2 + T_{mold}^2\right) \tag{14}$$

where $\sigma_{SB} = 5.6704 \cdot 10^{-8}\ \mathrm{W m^{-2} K^{-4}}$ is the Stefan-Boltzmann constant, $\varepsilon_{shell} = \varepsilon_{mold} = 0.8$ are the emissivities of the shell and mold surface, and T_{shell} and T_{mold} are their current temperatures, respectively. The conduction heat transfer coefficient depends on four resistances connected in series:

$$\frac{1}{h_{cond}} = \frac{1}{h_{mold}} + \frac{\left(d_{gap} - d_{slag}\right)}{k_{air}} + \frac{d_{slag}}{k_{slag}} + \frac{1}{h_{shell}} \tag{15}$$

The first resistance, $1/h_{mold}$, is the contact resistance between mold wall surface and the solidified mold slag film. The contact heat transfer coefficient h_{mold} is chosen to be 2500 W/m^2 (Park *et al.*, 2002). The second resistance is associated with conduction across the air gap assuming k_{air} = 0.06 W/m·K. The thickness of the air gap is determined from the results of the mechanical contact analysis. An artificial constant slag film thickness, d_{slag} = 0.1 mm, is adopted in this work to prevent non-physical behavior associated with very small gaps (Park *et al.*, 2002). The third resistance is due to conduction through the slag film assuming k_{slag} = 1 W/m·K. The final term is the contact resistance between the slag film and the strand, where the shell contact heat transfer coefficient h_{shell} depends greatly on temperature. This shell-slag contact coefficient decreases greatly as the shell surface temperature drops below the

solidification temperature of the mold slag (Han *et al.*, 1999). These equations were implemented into ABAQUS using the user-defined subroutine GAPCON (Dassault Corp., 2009).

The size of the gap is determined through the "softened" exponential contact algorithm built into ABAQUS/Standard (Dassault Corp., 2009), knowing the position of the mold wall and shell surfaces $\boldsymbol{x}_{mold}$ and $\boldsymbol{x}_{shell}$:

$$d_{gap}(t) = \left\| \boldsymbol{x}_{shell}(t) - \boldsymbol{x}_{mold}(\boldsymbol{p}, t) \right\| = \left\| \boldsymbol{x}_{shell}(t) - \boldsymbol{x}_{mold}(\boldsymbol{p}, z/V_c) \right\| \tag{16}$$

The first iteration of the shell model used the nominal shape of the mold. For the second iteration of the shell model, the mold model was post-processed to create a database of surface position, $\boldsymbol{x}_{mold}$, for points on the transverse perimeter of the hot face $\boldsymbol{p}$ and time below the meniscus $t = z/V_c$. A time-varying displacement was applied to each point on the hot face to re-create the distorted shape of the mold that the Lagrangian shell domain would encounter as it moves through the mold, using the ABAQUS user subroutine DISP.

8. Validation of the Numerical Models

The thermo-mechanical solidification model used in this work was validated by comparison with the semi-analytical solution of thermal stresses in an unconstrained solidifying plate (Weiner and Boley, 1963). A one-dimensional model of this test casting can produce the complete 3-D stress and strain state if the condition of generalized plane strain is imposed in both the width (y) and length (z) directions (Li and Thomas, 2004).

The domain adopted for this problem moves with the strand in a Lagrangian frame of reference as shown in Fig. 1. The domain consists of a thin slice through the plate thickness using 2-D 4-node generalized plane strain elements (in the axial z direction) implemented in ABAQUS. The second generalized plane strain condition was imposed in the y-direction (parallel to the surface) by coupling the displacements of all nodes along the bottom edge of the slice domain. A fixed temperature is imposed at the left boundary, with other boundaries insulated.

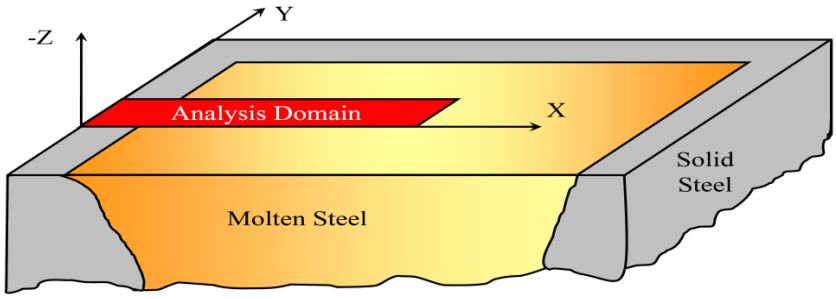

Figure 1: Solidifying Slice

The material in this problem has elastic-perfectly plastic constitutive behavior. The yield stress drops linearly with temperature from 20 MPa at 1000 ºC to zero at the solidus temperature 1494.4 ºC, which was approximated by σ_Y =0.03 Mpa at the solidus temperature. A very narrow mushy region, 0.1 ºC, is used to approximate the single melting temperature assumed in the analytical solution.

Figures 2 and 3 show the temperature and the stress distribution across the solidifying shell at two different solidification times. More details about this model validation can be found elsewhere (Koric and Thomas, 2006) including comparisons with other less-efficient integration methods and a convergence study.

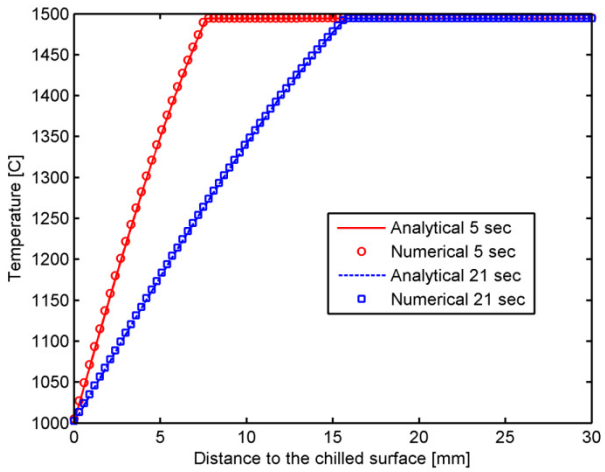

Figure 2: Temperature distribution along the solidifying slice

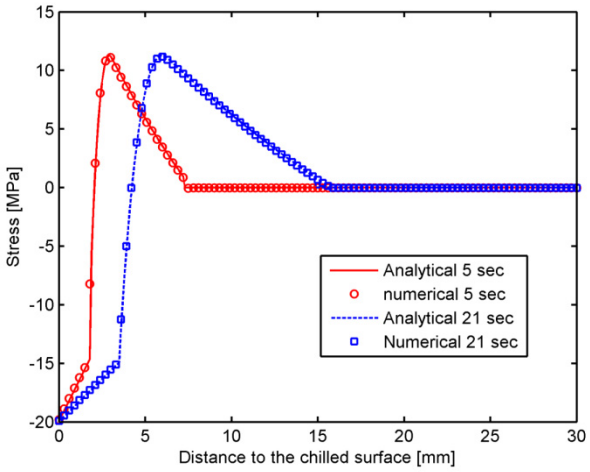

Figure: 3 Stress distributions along the solidifying slice

The method for modeling superheat by enhancing latent heat is also tested on the same slice domain and compared with a 1D analytical solution for conduction with phase change (Dantzig and Tucker, 2001). The superheat flux is best calculated with simultaneous modeling of fluid flow. Instead initial temperature is raised by 50 ºC, thus providing a superheat flux driven by the temperature difference between T_{init} and T_{liq} assuming stagnant liquid. Since the entire problem including the liquid pool starting from the initial temperature of T_{init} can be solved for this simplified test using the conventional solution method built into ABAQUS, the heat flux is extracted from that simulation as a function of time at the moving interface front (*i.e.* for the points that are at temperature T_{liq}). It represents the superheat flux entering the narrow mushy zone from the liquid pool. Next, the problem was rerun using the enhanced latent heat method in Abaqus with UMATHT. Here, the initial temperature is just above T_{liq}, thus providing no superheat through the temperature difference between T_{init} and T_{liq}. Instead, the latent heat enhancement needed in Eq. (9) was calculated from the superheat flux. A comparison of shell thickness (defined by T_{ref}) between the enhanced latent heat method, and the analytical solution is shown in Fig. 4, both with and without superheat. Naturally, solidification is faster with no superheat. The new enhanced latent heat method is demonstrated to accurately account for superheat in transient solidification problems.

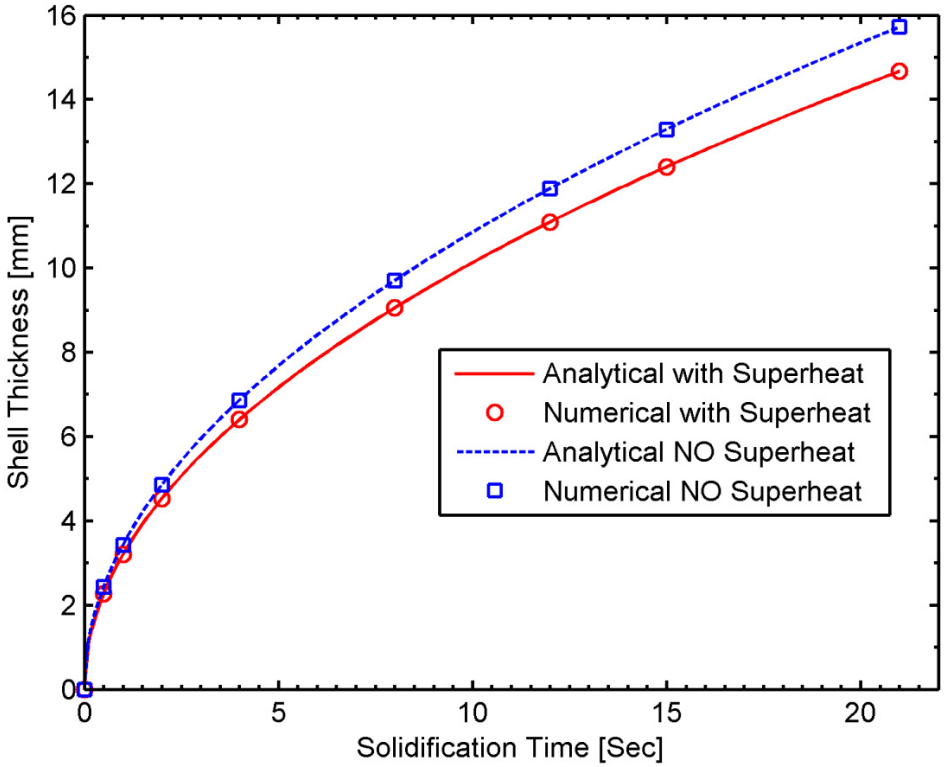

Figure 4: Shell Thickness History Comparison

9. Multiphysics Model of Beam Blank Casting

The entire multiphysics model was applied to solve for fluid-flow, temperature, stress, and deformation in a complex-shaped beam blank caster under realistic continuous casting conditions. Fig. 8 is a flow chart of the solution strategy for the thermo-mechanical-fluid flow model of steel continuous casting. First, the thermo-mechanical model of the solidifying shell is run assuming a uniform superheat distribution driven by the temperature difference between T_0 and T_{liq}, and artificially increasing thermal conductivity in the liquid region by 7-fold. The heat fluxes leaving the shell surface provide the boundary conditions for the thermo-mechanical model of the mold, which in turns supplies the next run of the shell model with mold temperature and thermal distortion boundary conditions. The position of the solidification front in the shell model defines an approximate shape of the liquid pool for the fluid flow model, which is used to calculate the superheat flux distribution. Finally, an improved thermo-mechanical model of solidifying

shell is re-run which includes the effects of the superheat distribution and mold distortion, and completes the first iteration of the multiphysics model. Because the shell profile from the improved thermo-mechanical model has little effect on superheat results in the liquid pool, a single multiphysics iteration is sufficient to produce an accurate shell growth prediction.

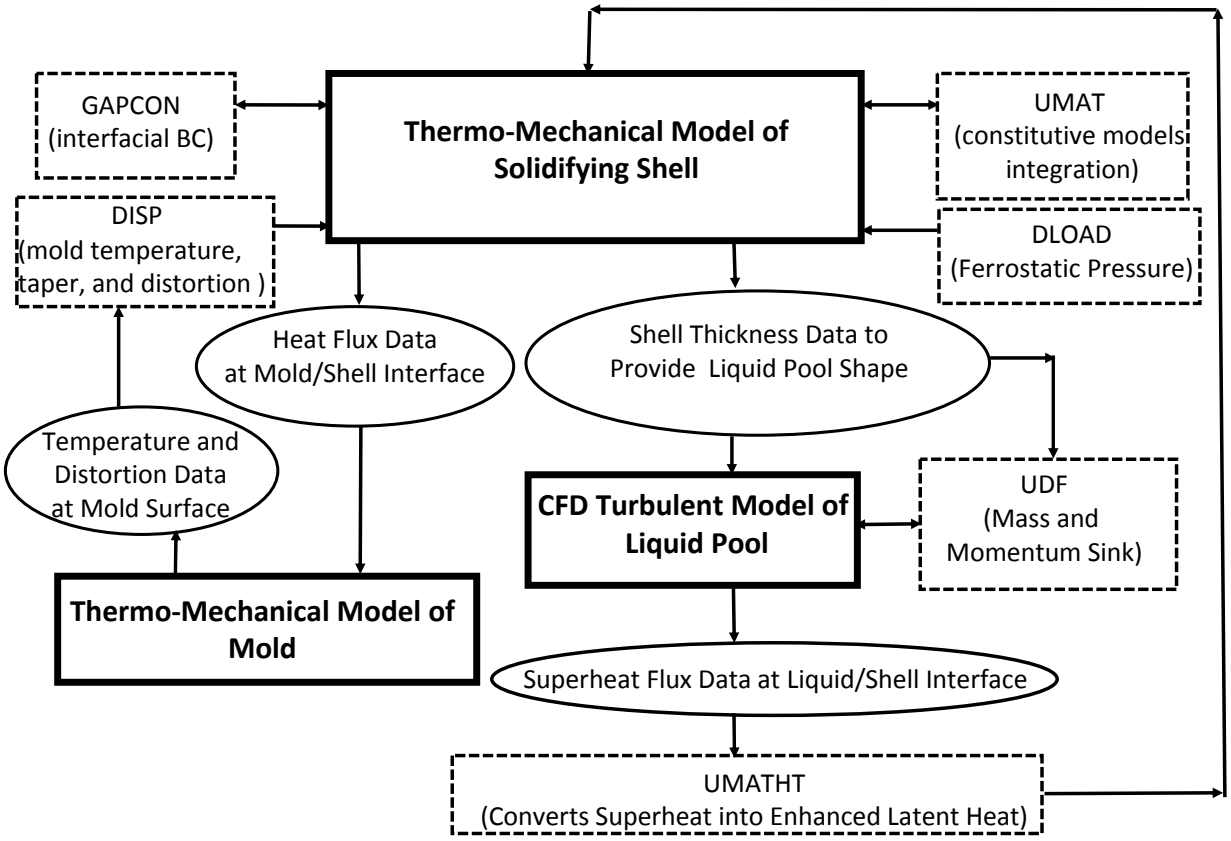

Figure 8: Flow Chart for Multiphysics Solution Strategy

The shoulder region of the beam-blank mold has a convex shape which converges heat flow and increases local temperature, opposite to behavior at the corners. Furthermore, a gap in the middle shoulder is caused by outward bending of the shell due to contact pressure from the mold onto the middle of the flange. Heat extraction from the shoulder is therefore retarded as shown in Fig. 10, yielding a thinner shell with higher temperature. The maximum and minimum principal stress contours at 457 mm (Hibbeler *et al.*, 2009) are given in Fig. 11. They reveal expected compressive shell behavior at the "cold" surface and tensile stress in the hot interior near the solidification front, similar to the model validation from Fig. 3. Maximum stress and strain is found in the shoulder area which is not a surprise since the thinner shell in

this region caused by gap formation leads to stress concentration. Longitudinal cracks and breakouts are often found in this same shoulder region, as revealed by plant observations (Hibbeler *et al.*, 2009).

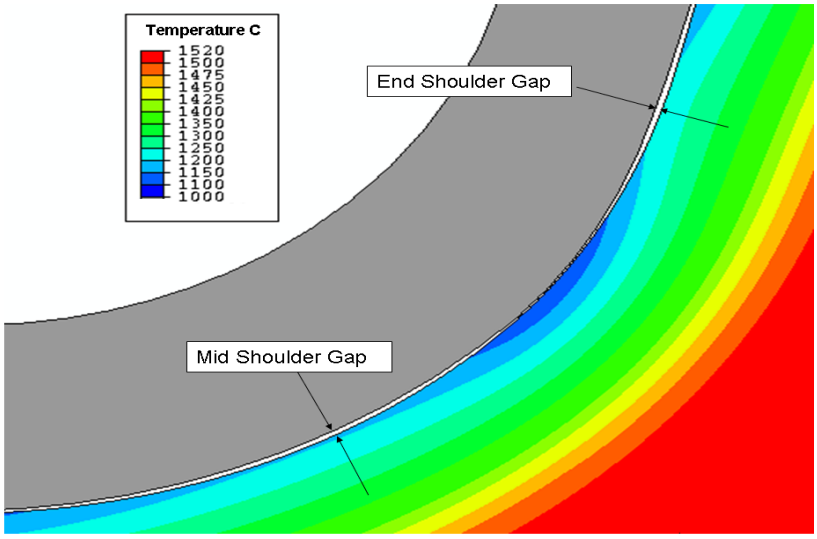

Figure 10: Beam-Blank Shoulder shell temperature contour with gap details

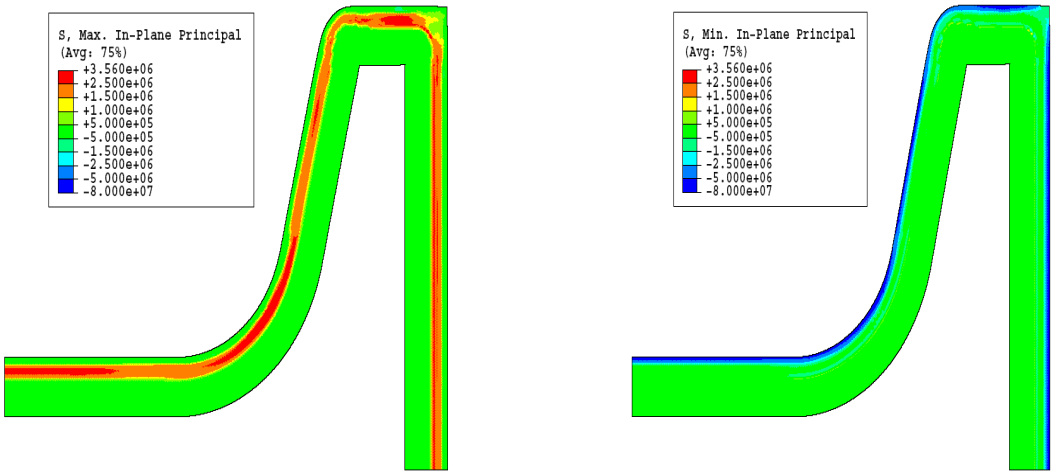

Figure 11: Max. and Min. Minimum principal stress contour 457 mm below meniscus

Finally, the shell thickness at 90% liquid predicted by both models is compared with measurements around the perimeter of a breakout shell obtained from a commercial caster (Hibbeler et al., 2009) in Figure 12. The initial thermo-mechanical model assuming a uniform superheat distribution can only roughly match the shell thickness variations. Shell thickness variations at the corners and shoulder due to air gap formations were captured owing to the interfacial heat transfer model. However, the middle portion of the wide face is 4 mm thicker in the measurement. This is evidently caused by the uneven superheat distribution due to the flow pattern in the liquid pool, as this location is farthest away from the pouring funnels and has the least amount of superheat as shown in Fig 9. In contrast, the shoulder region receives the highest amount of superheat, so the measured shell thickness there is more than 2 mm thinner than the initial thermo-mechanical model prediction. The improved multi-physics model that includes the fluid flow effects matches the shell thickness measurement around the entire perimeter much more accurately. This finding illustrates the improved accuracy that is possible by including the effects of fluid flow into a thermal stress analysis of solidifying shell.

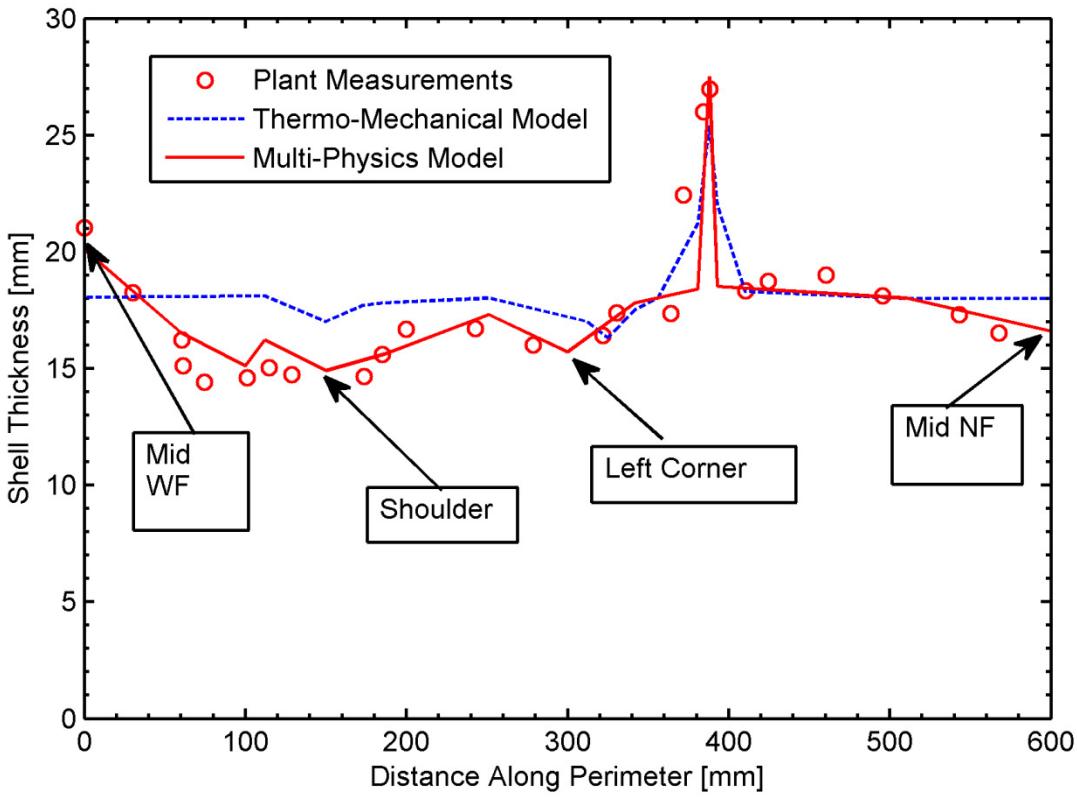

Figure 10: Shell Thickness Comparisons

10. Conclusions

The model developed in this work enables accurate uncoupling of complex multiphysics phenomena in continuous casting into separate simulations of the fluid flow region, the mushy zone and solid steel shell region, and the mold. Spatially and temporally non-uniform super heat fluxes, produced by turbulent fluid flow and mixing in the liquid pool, are calculated from the results of a finite-volume fluid flow model in FLUENT. A new latent-heat method is applied to link these results into a coupled thermo-mechanical model of continuous casting using a finite-element model in ABAQUS. The realistic effect of mold thermal distortion is incorporated through a second database and boundary condition at the shell-mold interface. The model is first validated with available analytical solutions of thermal stress, temperature, and shell growth. The model is then applied to simulate solidification in a one-quarter transverse section of a commercial beam blank caster with complex geometry, temperature dependent material properties, and realistic operating conditions. The results compare well with in-plant measurements of the thickness of the solidifying shell.

This paper illustrates an effective approach towards accurate multiphysics modeling of commercial processes. By exploiting unique features of the continuous casting of steel, individual models can be coupled together in an efficient, accurate, and robust way to achieve realistic predictions of metal solidification on the continuum scale. The key is the careful choice of the boundaries between modeling domains, and their treatment in both connecting models, such that convergence can be achieved in as little as one iteration on the macroscale. The most intimately-coupled phenomena are modeled in the same domain and model. In particular, the coupling between heat transfer across the shell mold gap and shrinkage are simulated together in the shell model.

Realistic prediction of shell shape, temperature, and shrinkage is just the first step in predicting the formation of defects such as porosity, segregation, and cracks, microstructure, and final properties. Much further work remains to incorporate further models of these additional phenomena into useful modeling systems, tailored for a given commercial process.

Acknowledgements

The authors would like to thank Clayton Spangler and the Steel Dynamics Structural and Rail Mill in Columbia City, Indiana for their great support for this project, and the National Center for Supercomputing Applications (NCSA) for computational and software resources. Funding of this work

by the Continuous Casting Consortium at the University of Illinois and the National Science Foundation Grant # CMMI 07-27620 is gratefully acknowledged.

References

Weiner, J. H., Boley, B. A., 1963. Elasto-plastic thermal stresses in a solidifying body. J. Mech. Phys. Solids. 11,145-154.

Koric, S., Thomas, B. G., Voller, V. R., 2010. Enhanced Latent Heat Method to Incorporate Superheat Effects into Fixed-grid Multiphysics Simulations. Numerical Heat Transfer Part B, In Press

Koric, S., Thomas, B. G., 2006. Efficient Thermo-Mechanical Model for Solidification Processes. International Journal for Num. Methods in Eng., 66, 1955-1989.

Dantzig, J. A., Tucker III, C. L, 2001. Modeling in Materials Processing, First ed. Cambridge University Press, Cambridge, UK.

Zhu, H., 1993. Coupled thermal-mechanical finite-element model with application to initial solidification. Ph.D Thesis University of Illinois.

Li, C., Thomas B.G., 2004. Thermo-Mechanical Finite-Element Model of Shell Behavior in Continuous Casting of Steel. Metal. & Material Trans. B., 35B(6), 1151-172.

Grill, A., Brimacombe, J. K, Weinberg, F., 1976. Mathematical analysis of stress in continuous casting of steel. Ironmaking Steelmaking, 3, 38-47.

Rammerstrofer, F. G.,Jaquemar, C., Fischer, D. F, Wiesinger, H., 1979. Temperature fields, solidification progress and stress development in the strand during a continuous casting process of steel. Numerical Methods in Thermal Problems, Pineridge Press, 712-722.

Kristiansson, J. O., 1984. Thermomechanical behavior of the solidifying shell within continuous casting billet molds- a numerical approach. *Journal* of Thermal Stresses, 7, 209-226.

Boehmer, J. R., Funk, G., Jordan, M., Fett, F. N., 1998. Strategies for coupled analysis of thermal strain history during continuous solidification processes. Advances in Engineering Software, 29 (7-9), 679-97.

Risso, J.M., Huespe, A. E., Cardona, A., 2005. Thermal stress evaluation in the steel continuous casting process. International Journal of Numerical Methods in Engineering, 65(9), 1355-1377.

Koric, S., Hibbeler, C., L.,Thomas, B., G., 2009. Explicit coupled thermo-mechanical finite element model of steel solidification, International Journal of Numerical Methods in Engineering ,78, 1-31.

Hibbeler, C., L., Koric, S., Xu, K.,Spangler, C.,Thomas, B., G., 2009. Thermomechanical Modeling of Beam Blank Casting. Iron and Steel Technology,6(7),60-73.

Lee, J., Yeo, T.,,Kyu, OH, K., H., J. Yoon, J., Yoon, U., 2000. Prediction of Cracks in Continuously Cast Steel Beam Blank through Fully Coupled Analysis of Fluid Flow, Heat Transfer, and Deformation Behavior of a Solidifying Shell. Metal. and Materials Transactions A, 31A, 225-237.

Teskeredzic, A.,Demirdzic, I.,Muzaferija, S., 2002. Numerical method for heat transfer, fluid flow, and stress analysis in phase-change problems. Numerical Heat Transfer B, 42(5), 437-459.

Shamsi, M. R., Ajmani, S. K, 2008. Three Dimensional Turbulent Fluid Flow and Heat Transfer Mathematical Model for the Analysis of a Continuous Slab Caster. ISIJ International, 47(3), 433-442.

Pokorny, M., Monroe, C., Beckermann, C., Bichler, L., Ravindran, C., 2008. Prediction of Hot Tear Formation in Magnesium Alloy Permanent Mold Casting,. Int. J. Metalcasting, 2(4), 41-53.

Ho, K., Pehlke, R., D., 1985. Metal-Mold interfacial heat transfer. Metallurgical Transactions B, 16(3), 585-594.

ABAQUS User Manuals v. 6.9, 2009. Dassault Systems Simulia Corp., Providence, RI.

Kozlowski, P., F., Thomas, B., G., Azzi, J. A., Wang, H. 1992. Simple constitutive equations for steel at high temperature. Metallurgical Transactions, 23A, 903-918.

Voller, V., R., Prakash, C., 1987. A Fixed-Grid Numerical Modeling Methodology for Convection-Diffusion Mushy Region Phase-Change Problems. Int. J. Heat Mass Transfer, 30, 1709-1720.

Versteeg, H. K., Malalasekera, W., 2008. An Introduction to Computational Fluid Dynamics, Second Ed., Pearson Prentice Hall, New York, NY.

Fluent User Manuals v6.3, 2008. Ansys Inc.,Canonsburg, PA.

Rietow, B., 2007. Fluid Velocity Simulations and Measurements in Thin Slab Casting. MS Thesis, University of Illinois.

Launder, B. E., Spalding, D., B., 1974. The Numerical Computation of Turbulent Flows. Comput. Methods Appl. Mech. Eng., 3, 269-289.

Park, J., K., Thomas, B., G., Samarasekera, I., 2002. Analysis of Thermo-Mechanical Behavior in Billet Casting with Different Mold Corner Radii. Ironmaking and Steelmaking, 29(5), 359-375.

Han, H. N., Lee, J. E., Yeo, T. J., Won, Y. M., Kim, K., Oh, K., H., Yoon, J. K. 1999. A Finite Element Model for 2-Dimensional Slice of Cast Strand. ISIJ International,39(5),445-455.

Table I: Constants Used in Validation Test Problems

Thermal Conductivity [W/m·K]	33
Specific Heat Capacity [J/kg·K]	661
Elastic Modulus in Solid [GPa]	40
Elastic Modulus in Liquid [GPa]	14
Thermal Linear Expansion Coefficient [1/K]	0.00002
Mass Density [kg/m³]	7500
Poisson's Ratio	0.3
Liquidus Temperature [ºC]	1494.45
Fusion Temperature (analytical) [ºC]	1494.4
Solidus Temperature [ºC]	1494.35
Initial Temperature, no superheat [ºC]	1495
Initial Temperature, with superheat [ºC]	1545
Latent Heat of Fusion [J/kg·K]	272000
Surface Temperature [ºC]	1000

Table II Beam Blank Simulation Conditions

Strand section size (mold top) [mm]	576 x 436 x 93
Working Mold length [mm]	660.4
Total taper at flange [mm]	2.33
Total taper at sloped shoulder edge [mm]	-2.22
Total taper at wide face [mm]	0.48
Total taper at narrow face [mm]	3.0
Mold contact resistance feat coefficient, h_{mold} [$W/m^2/K$]	2500
Casting speed [m/min]	0.889
Mold Thermal Conductivity (Copper) [W/m·K]	370
Steel grade [% wt. C]	0.071
Initial temperature strand [ºC]	1523.70
Initial temperature mold [ºC]	285
Liquidus temperature [ºC]	1518.70
Solidus temperature [ºC]	1471.95
Cooling water temperature [ºC]	34.5

Table III Fluid Flow Input Data

Density (kg/m^3)	ρ	**6800**
Kinetic Viscosity (m^2/s)	v	**0.006**
Inlet Velocity (m/s)	v_{in}	**1.854**
Inlet Diameter (m)	d	**0.0255**
Turbulence intensity at inlet (%)	I	**200**
Inlet kinetic energy (kg*m^2/s^2)	K	**0.464**
Inlet dissipation rate (m^2/s^3)	ε	**2.077**
Area of inlet flow (m^2)	A_{in}	**2.56×10^{-4}**
Area of outflow (m^2)	A_l	**0.0215**
Area of top surface (m^2)	A_m	**0.032**
Casting Speed (m/s)	v_C	**0.0148**